Acta Cryst. (1993). A**49**, 818–824

X-ray Interference on Finite Polyhedral Crystals

By A. A. Snigirev and A. Yu. Suvorov

Institute of Microelectronics Technology and High-Purity Materials, Russian Academy of Sciences, 142432 *Chernogolovka, Moscow District, Russia*

(*Received* 10 *November* 1992; *accepted* 15 *April* 1993)

Abstract

An X-ray interference phenomenon associated with the superposition of reflected waves corresponding to the different diffraction types may be observed for finite polyhedral crystals. Using plane-wave solutions, the interference patterns are analyzed for the two specific geometries of the crystal profile. The computer simulations supplement the theoretical inferences and fit the experimental results.

Introduction

Theoretical analysis of X-ray diffraction on crystals with arbitrary boundary conditions is a very complicated problem within the framework of the dynamic theory. Although research in this area has been hard to realize experimentally, a few studies have contributed significantly to the theoretical and experimental investigation of diffraction geometries different from the conventional Bragg and Laue ones (Becker & Dunstetter, 1984; Lehmann & Borrmann, 1967; Saka, Katagawa & Kato, 1972*a*,*b*; Uragami, 1969, 1970, 1971). The most convenient classification and terminology for the possible geometries of X-ray diffraction by finite polyhedral crystals were provided by Saka, Katagawa & Kato (1972*a*,*b*), together with a complete theory for plane- and spherical-wave approximations. Amongst other things, the spherical-wave solutions obtained completely described the so-called Borrmann–Lehmann interference effect and facilitated treatment of the experimental data (Lang, Kowalski & Makepeace, 1990).

As discussed by Saka, Katagawa & Kato (1972*a*), the Laue–Bragg diffraction geometry under which Borrmann–Lehmann interference fringes have been generated is just the simplest member of a family of geometries involving Laue-case boundary conditions at the entrance surface and Bragg-case boundary conditions at the exit surface. Previously, the fabrication of specimens suitable for experiments of this type faced technological difficulties that can now be overcome by using procedures such as photolithography, ion-plasma etching and anisotropic etching. Very interesting experimental results from the observation of diffracted-wave spectra from a periodic single-crystal structure were recently presented by Aristov *et al.* (1988). Sufficiently high diffraction-pattern contrast was revealed and the so-called 'thickness oscillations' of the main peak were recorded. The interpretation of the observed effects was made from the viewpoint of the kinematical theory. The surface profiling of silicon single crystals was successfully used for the fabrication of Bragg–Fresnel zone plates, on which focusing and image transmission of a periodic object were obtained (Aristov *et al.*, 1992).

The above created a need for more careful research into X-ray diffraction in polyhedral crystals. This paper presents experimental topographs of crystals with rectangular edge and rectangular surface profiles as well as analytical interpretation and computer simulation of the observed interference phenomena.

Diffraction geometry

Because the diffraction geometries involved fall within the classification given by Saka *et al.* (1972*a*), their terminology is used. In the first case, illustrated in Fig. 1(*a*), a plane wave illuminates the crystal, whose facets are perpendicular (*AB*) and parallel (*BC*) to the reflecting planes. Consequently, one has symmetric Bragg diffraction on the top surface, *BC*, and symmetric Laue–Bragg diffraction on the lateral surface, *AB*. The incident-wave direction is defined by the vacuum wave vector $\mathbf{K}_0$, while the direction of the diffracted wave is taken as $\mathbf{K}_h = \mathbf{K}_0 + \mathbf{h}$, where $\mathbf{h}$ is the reciprocal-lattice vector. For the given geometry, the interest lies in the intensity distribution along the exit surface *BC*, which involves the superposition of Bragg and Laue–Bragg waves.

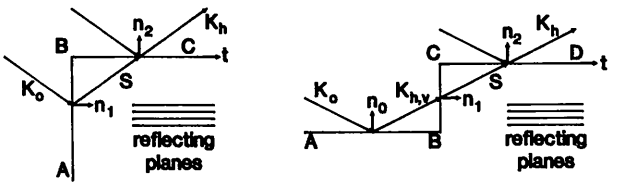

(*a*) (*b*)

Fig. 1. Illustrations of the geometry of the crystal profiles: (*a*) type *A*; (*b*) type *B*.

©1993 International Union of Crystallography
Printed in Great Britain – all rights reserved

ISSN 0108-7673 ©1993

The second geometry, shown in Fig. 1(*b*), comprises a more complicated configuration of surfaces, of which two (*AB* and *CD*) are parallel to the reflecting planes and one (*BC*) is perpendicular. Consideration is restricted to the intensity distribution along the initial part of the surface *CD*, which is the most interesting location of wave-field superposition because one obtains a combination of three diffraction types at once: Bragg–Bragg, Laue–Bragg type I and Laue–Bragg type II. This geometry is of particular interest because under certain conditions it makes possible the interference of two Bragg–Bragg waves virtually without any influence from Laue–Bragg diffraction. This may occur because the exact angular positions for the Bragg and Laue cases are displaced with respect to each other by $\Delta\Theta = \chi_0/\sin(2\theta_B)$. In this case, the optical path difference between the waves reflected from the top and bottom facets depends on the height of the ridge, H_r, and on the deviation from the Bragg condition. Consequently, this geometry may be considered to be analogous to that of an optical interferometer and may be used for the determination of the X-ray coherency.

Plane-wave solution

The plane-wave solutions for the wave fields inside a crystal and for waves coming out of a crystal in the Laue–Bragg case (types I and II) were thoroughly considered by Saka *et al.* (1972*a*). In this case, it is suggested that all reflections associated with the appropriate diffraction types are symmetric. In Fig. 1, unit vectors $\mathbf{n}_0$, $\mathbf{n}_1$ and $\mathbf{n}_2$ denote the normals to the corresponding facets. Let a plane monochromatic X-ray wave of unit amplitude $\exp(i\mathbf{K}_0\cdot\mathbf{r})$ be incident on a crystal. Then, for the Laue–Bragg case of type I, the wave emerging from the exit surface is

$$E_{\rm I}(\mathbf{r}_2) = C_{\mathbf{h}}\exp[i\mathbf{K}_{\mathbf{h}}\cdot\mathbf{r}_1 + i\mathbf{k}_{\mathbf{h}}\cdot(\mathbf{r}_2-\mathbf{r}_1)] \quad (1a)$$

$$C_{\mathbf{h}} = \mp\eta[\eta\pm(1+\eta^2)^{1/2}]/(1+\eta^2)^{1/2} \quad (1b)$$

$$\eta = (\theta_B-\theta)\sin(2\theta_B)/\tilde{\chi}_{\mathbf{h}},\quad \tilde{\chi}_{\mathbf{h}} = C(\chi_{\mathbf{h}}\chi_{-\mathbf{h}})^{1/2}, \quad (1c)$$

where positive and negative signs correspond to branch (1) and branch (2) waves, respectively, and the vectors $\mathbf{r}_1$ and $\mathbf{r}_2$ indicate positions on the crystal surfaces *AB* and *BC*, respectively. For the sake of simplicity, the Fourier coefficients of the polarizability, χ_0, $\chi_{\mathbf{h}}$, $\chi_{-\mathbf{h}}$, are assumed to be real. The wave vector $\mathbf{k}_{\mathbf{h}}$ is related to $\mathbf{K}_0$ by

$$\mathbf{k}_{\mathbf{h}} = \mathbf{k}_0 + \mathbf{h}, \quad (2a)$$

$$\mathbf{k}_0 = \mathbf{K}_0 - K\delta_0\mathbf{n}_1, \quad (2b)$$

$$K\delta_0 = -(K\chi_0/2\cos\theta_B) - (K\tilde{\chi}_{\mathbf{h}}/2\cos\theta_B) \times[-\eta\pm(1+\eta^2)^{1/2}]. \quad (2c)$$

At the exact Bragg position ($\eta = 0$), the wave fields corresponding to the different dispersion surface branches are totally reflected from the exit surface, so that no intensity comes out from the crystal. When $\eta \neq 0$, just one Bloch wave gives rise to the vacuum wave; namely, the one with the Poynting vector directed toward the exit surface. The second solution (Saka *et al.*, 1972*a*) may be considered as a hypothetical reflection from an imaginary extension of the exit surface. Therefore, there is only one physically significant solution, which is

$$C_{\mathbf{h}} = \begin{cases} C_{\mathbf{h}}^{(2)} & \text{for } \eta > 0 \\ C_{\mathbf{h}}^{(1)} & \text{for } \eta < 0 \end{cases}. \quad (3)$$

From (2*a*)–(2*c*), (1*a*) can be rewritten as

$$E_{\rm I}(\mathbf{r}_2) = C_{\mathbf{h}}\exp[-iK\delta_0\mathbf{n}_1\cdot(\mathbf{r}_2-\mathbf{r}_1) + i\mathbf{K}_{\mathbf{h}}\cdot\mathbf{r}_2]. \quad (4)$$

Let us introduce the position parameter t, the distance from the observation point on the exit surface to the crystal edge:

$$t = (\mathbf{r}_2-\mathbf{r}_1)\cdot\mathbf{n}_1. \quad (5)$$

Then, (4) can be rewritten as

$$E_{\rm I}(\mathbf{r}_2) = C'_{\mathbf{h}}\exp(i\mathbf{K}_{\mathbf{h}}\cdot\mathbf{r}_2), \quad (6a)$$

$$C'_{\mathbf{h}} = C_{\mathbf{h}}\exp(-iK\delta_0 t). \quad (6b)$$

For the Laue–Bragg case of type II, the wave emerging from the exit surface is

$$E_{\rm II}(\mathbf{r}_2) = C_0\exp[i\mathbf{K}_0\cdot\mathbf{r}_1 + i\mathbf{k}_0\cdot(\mathbf{r}_2-\mathbf{r}_1)], \quad (7a)$$

$$C_0 = \pm\eta/(1+\eta^2)^{1/2}. \quad (7b)$$

Similar reasoning shows that

$$C_0 = \begin{cases} C_0^{(1)} & \text{for } \eta > 0 \\ C_0^{(2)} & \text{for } \eta < 0 \end{cases}. \quad (8)$$

Likewise, (7*a*) can be rewritten as

$$E_{\rm II}(\mathbf{r}_2) = C'_0\exp\{i\mathbf{K}_0\cdot\mathbf{r}_2\}, \quad (9a)$$

$$C'_0 = C_0\exp\{-iK\delta_0 t\}. \quad (9b)$$

The plane-wave solution for the Bragg case is well known and can be written as

$$E_B(\mathbf{r}_2) = C_B\exp(i\mathbf{K}_{\mathbf{h}}\cdot\mathbf{r}_2), \quad (10a)$$

$$C_B = \begin{cases} \beta - i(1-\beta^2)^{1/2}, & |\beta|\le 1 \\ \beta\mp(\beta^2-1)^{1/2}, & |\beta|>1 \end{cases}, \quad (10b)$$

$$\beta = \chi_0/\tilde{\chi}_{\mathbf{h}} - \eta, \quad (10c)$$

where the upper sign corresponds to $\beta > 1$ and the lower sign corresponds to $\beta < -1$. The exact Bragg position in this case is determined as $\beta = 0$, *i.e.*

$$\theta = \theta_B - \chi_0/\sin(2\theta_B), \quad (11)$$

which is due to the refraction of the incident wave on the crystal boundary.

Let us now consider the diffraction geometry illustrated in Fig. 1(*a*). The wave emerging from the exit surface *BC* is a superposition of Bragg and Laue–Bragg wave fields. Hence, it can be written as

$$E_{\mathbf{h}}(\mathbf{r}_2) = (C_B + C'_{\mathbf{h}}) \exp(i\mathbf{K}_{\mathbf{h}} \cdot \mathbf{r}_2). \quad (12)$$

If diffraction occurs in the region $|\beta| > 1$, then the intensity is

$$I_{\mathbf{h}}(t) = C_B^2 + C_{\mathbf{h}}^2 + 2C_B C_{\mathbf{h}} \cos(K\delta_0 t). \quad (13)$$

Thus, the intensity of the outcoming wave is modulated with a period

$$D = 2\pi/|K\delta_0|. \quad (14)$$

It is readily seen that there is a point η_0 where the period turns into infinity, *i.e.* $K\delta_0 = 0$,

$$\eta_0 = -(\xi^2 - 1)/2\xi, \quad \xi = -\chi_0/\tilde{\chi}_{\mathbf{h}}. \quad (15)$$

With increase in the deviation ($|\eta| \to \infty$), the period decreases and tends to zero.

In the angular region $|\beta| < 1$, the diffracted intensity is

$$I_{\mathbf{h}}(t) = 1 + C_{\mathbf{h}}^2 + 2C_{\mathbf{h}} \sin(\psi + K\delta_0 t), \quad (16a)$$

$$\psi = \arctan[\beta/(1 - \beta^2)^{1/2}]. \quad (16b)$$

Thus, the period of the oscillations is identical to (14) but the location of the interference maxima depends additionally on the position inside the angular region through the phase parameter ψ.

Investigating the second diffraction geometry, one should take into account the fact that the wave reflected from the surface *AB* propagates in a vacuum with the wave vector $\mathbf{K}_{\mathbf{h},\mathbf{v}}$ (see Fig. 1*b*). Therefore, on the surface *BC*, this wave appears as

$$E(\mathbf{r}_1) = C_B \exp\{i\mathbf{K}_{\mathbf{h},\mathbf{v}} \cdot (\mathbf{r}_1 - \mathbf{r}_0) + i\mathbf{K}_{\mathbf{h}} \cdot \mathbf{r}_0\}, \quad (17a)$$

$$\mathbf{K}_{\mathbf{h},\mathbf{v}} = \mathbf{K}_{\mathbf{h}} - K\delta_{\mathbf{h}}\mathbf{n}_0, \quad (17b)$$

$$K\delta_{\mathbf{h}} = [K\tilde{\chi}_{\mathbf{h}}/\sin(\theta_B)]\eta, \quad (17c)$$

where $K\delta_{\mathbf{h}}$ is a linear approximation defined from the condition $|\mathbf{K}_0| = |\mathbf{K}_{\mathbf{h},\mathbf{v}}| = 2\pi/\lambda$. Consequently, the wave on the surface *CD* is defined as

$$E_{\mathrm{II}}(\mathbf{r}_2) = \tilde{C} \exp(i\mathbf{K}_{\mathbf{h}} \cdot \mathbf{r}_2), \quad (18a)$$

$$\tilde{C} = C_B C_0 \exp(-iK\delta_0 t - iK\delta_{\mathbf{h}} H_r), \quad (18b)$$

$$H_r = (\mathbf{r}_2 - \mathbf{r}_0) \cdot \mathbf{n}_0. \quad (18c)$$

The combined wave field is made up of three waves:

$$E_{\mathbf{h}}(\mathbf{r}_2) = E_B(\mathbf{r}_2) + E_{\mathrm{I}}(\mathbf{r}_2) + E_{\mathrm{II}}(\mathbf{r}_2). \quad (19)$$

It is easily seen that at sufficiently large deviation, $|\eta| \gg 1$, the influence of the Laue–Bragg case upon the interference pattern is negligible while the Bragg intensity may still be strong or even a maximum. This can be achieved, for instance, by choosing high-order reflections. Then, the exact Bragg position $\beta = 0$ corresponds to $\eta_B = \chi_0/\tilde{\chi}_{\mathbf{h}}$, which may be well above unity. In this approximation, the intensity of the reflected wave is

$$I_{\mathbf{h}}(t) \simeq 4|C_B|^2 \cos^2[\tfrac{1}{2}(\Delta K t + K\delta_{\mathbf{h}} H_r)], \quad (20a)$$

$$\Delta K = -K\chi_0/2\cos(\theta_B). \quad (20b)$$

Hence, the outcoming intensity is fully modulated in amplitude with the period

$$D_B = 2\pi/|\Delta K| \quad (21a)$$

and the initial phase is

$$\varphi_0 = K\delta_{\mathbf{h}} H_r. \quad (21b)$$

In a general case, the periodicity of the interference pattern is conserved but the oscillation amplitude depends on the particular reflection parameters in a more complicated way. The distinctive property of this geometry is that the period of the oscillations may not become infinite and for $|\eta| \gg 1$ becomes constant [(21*a*)].

Experiment and simulation

The experiments were performed using Cu $K\alpha$ radiation and a parallel double-crystal scheme. The

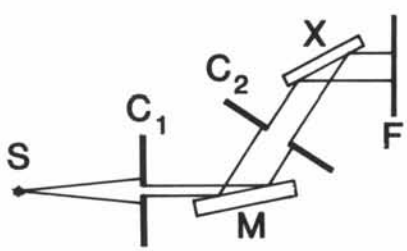

Fig. 2. The experimental scheme: *S* represents the source; C_1 and C_2 indicate the slits; *M* is the monochromator; *X* is the specimen; and *F* is the photoplate.

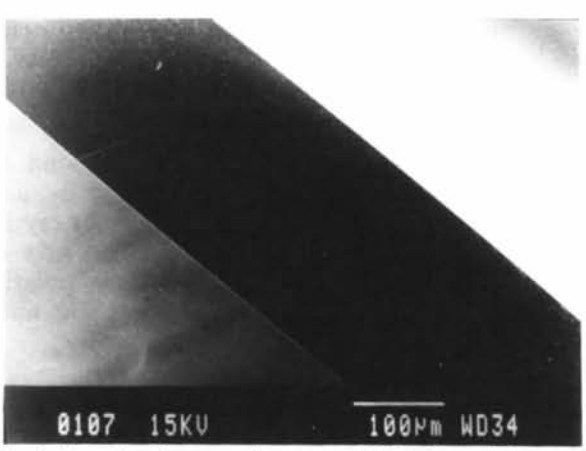

Fig. 3. Scanning electron microscope (SEM) view of the lateral surface of the silicon wafer prepared for the type-*A* diffraction setting (*cf.* Fig. 1*a*). Crystal thickness $T = 250\ \mu$m.

general layout of the experiments is shown schematically in Fig. 2. In the case of the first diffraction geometry (Fig. 1*a*), the symmetric 220 reflection from the sample and the asymmetric 220 reflection from the monochromator with the asymmetry factor $b = \gamma_h/\gamma_o \simeq 37$ were used. The rectangular edge was fabricated from a dislocation-free single-crystal silicon wafer by traditional methods of photolithography and subsequent anisotropic etching (Fig. 3). Fig. 4 shows magnified parts of the topographs taken at various angular positions. The relevant computer simulation is shown in Fig. 5. Because of the photoelectric absorption, the amplitude of the interference oscillations decreases with distance from the crystal edge. Also, the unpolarized radiation gives rise to periodical beats of the fringe intensity similar to the polarization beats of the Pendellösung fringes in the Laue–Laue case. Both effects lead to the rapid deterioration of the fringe visibility away from the edge.

From the pictures obtained, it is readily seen that the fringe period tends to widen as the deviation parameter decreases ($\eta \to 0$). For the given experimental conditions and polarized radiation, the fringe period turns into infinity at $\eta_0 = -0.5$ ($\Delta\theta = -1.24''$), while the exact Bragg position ($\beta = 0$) corresponds to $\eta_B = -1.65$ ($\Delta\theta = -4.1''$). Thus, the topograph shown in Fig. 4(*a*) was taken in the vicinity of η_0 and, consequently, the tendency towards a decreasing fringe period agrees with the theoretical inference. The period of the fringes in Fig. 4(*d*) is in agreement with that calculated and displayed in Fig. 5(*d*) and has $D \simeq 3.7$ μm in a registration plane. The dependence of the interference fringes on the deviation parameter, obtained from the computer simulation, is demonstrated in Fig. 6. The plots were calculated taking into account photoelectric absorption and unpolarized incident radiation.

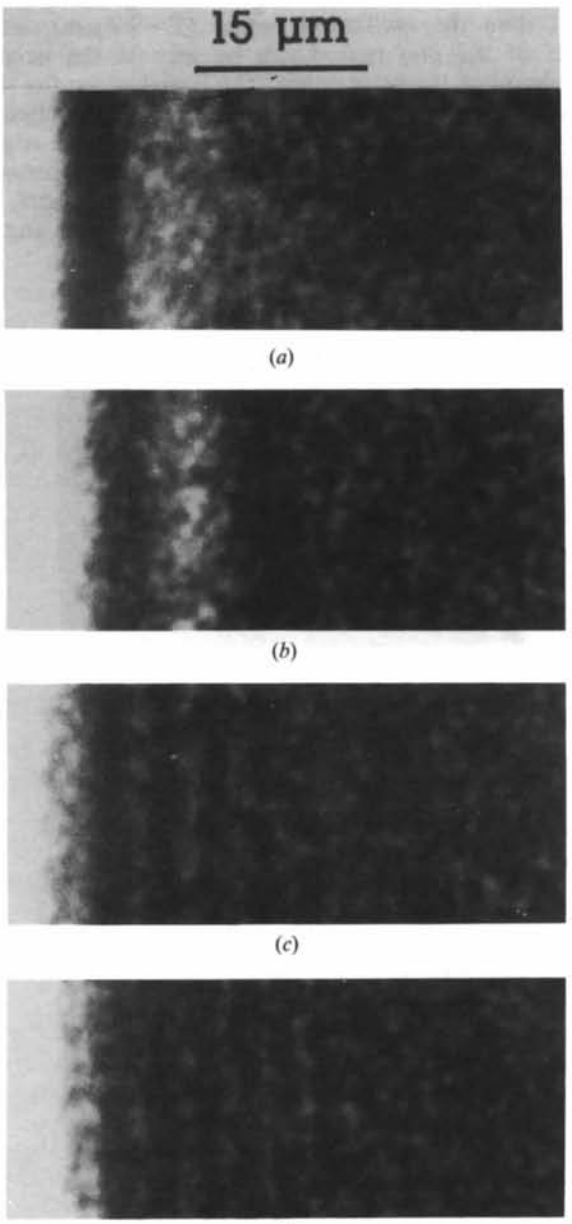

Fig. 4. Observed topographs showing interference fringes in the type-*A* diffraction setting (*cf.* Fig. 1*a*). (*a*) $\eta = -0.32$; (*b*) $\eta = -1.25$; (*c*) $\eta = -2.13$; (*d*) $\eta = -2.5$.

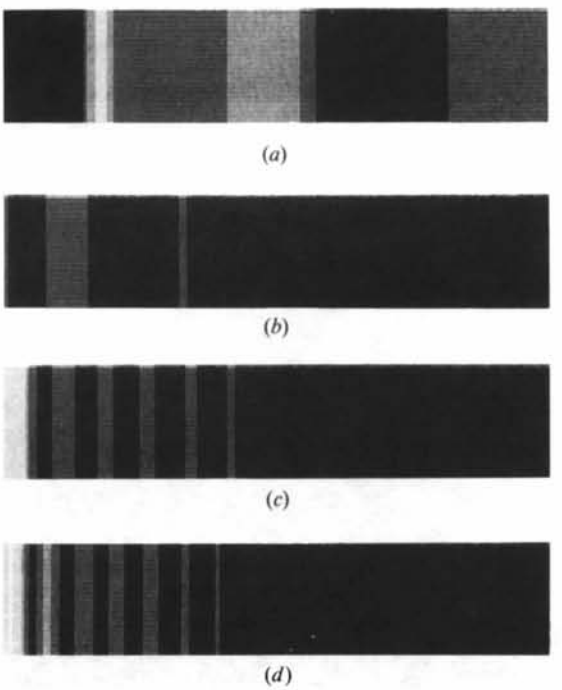

Fig. 5. Simulated topographs showing interference fringes in the type-*A* setting (*cf.* Fig. 1*a*). (*a*) $\eta = -0.32$; (*b*) $\eta = -1.25$; (*c*) $\eta = -2.13$; (*d*) $\eta = -2.5$.

To realize the diffraction geometry illustrated in Fig. 1(*b*), the periodical relief fabricated on the single-crystal silicon wafer by photolithography and subsequent reactive ion-plasma etching was used. The experimental conditions were as follows: monochromator with 511 reflection and asymmetry factor $b \simeq 12$; sample with 333 reflection, relief period $D_r = 60\ \mu m$ (width of ridge $\simeq 30\ \mu m$) and relief height $H_r \simeq 10\ \mu m$ (Fig. 7). The reflection used makes it possible to suppress π polarization and separate clearly the exact positions for Bragg and Laue cases because the angular spacing between them is $\Delta\Theta \simeq 3''$ while the width of the rocking curve is $\omega_s \simeq 2''$.

Fig. 8 shows topographs taken at three angular positions of the crystal, where the left half of each image corresponds to the reflection from the crystal substratum. At $\beta = 0$ (Fig. 8*a*), the deviation parameter is $\eta_B \simeq -3.4$ and, therefore, it is conceivable that only the Bragg case significantly affects the interference pattern. The fringe period in this instance is $D_B = 13.8\ \mu m$ along the exit surface. Because the interference region $T = H_r / \tan(\theta_B)$ is less than the oscillation period ($T \simeq 9.2\ \mu m$), only half of the first period can be seen in the neighborhood of the ridge edges. The initial phase for the given relief height is $\varphi_0 \simeq 2.6\pi$, *i.e.* there is actually no shift of fringes with reference to the ridge edge. To displace the interference fringes by one period, the increment of the ridge height must be $\Delta H_r = 2\pi/|K\delta_{\mathbf{h}}|$, that is $\Delta H_r \simeq 7.5\ \mu m$ at $\beta = 0$, or the angu-

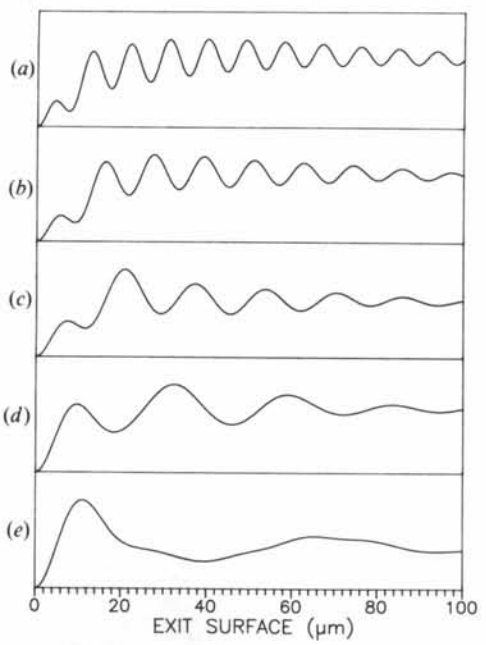

Fig. 6. Computed intensity profiles in the case of type-*A* setting (*cf.* Fig. 1*a*), Cu $K\alpha$ radiation and 220 reflection. (*a*) $\eta = -2.45$; (*b*) $\eta = -2.05$; (*c*) $\eta = -1.65$; (*d*) $\eta = -1.25$; (*e*) $\eta = -0.85$.

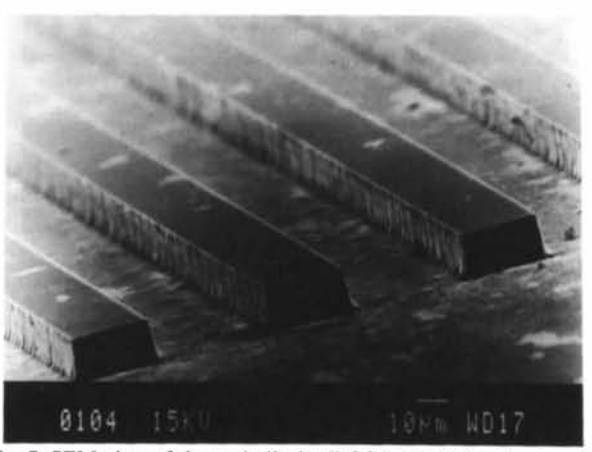

Fig. 7. SEM view of the periodical relief fabricated for the type-*B* diffraction setting (*cf.* Fig. 1*b*). Period $D \simeq 60\ \mu m$, height $H_r \simeq 10\ \mu m$.

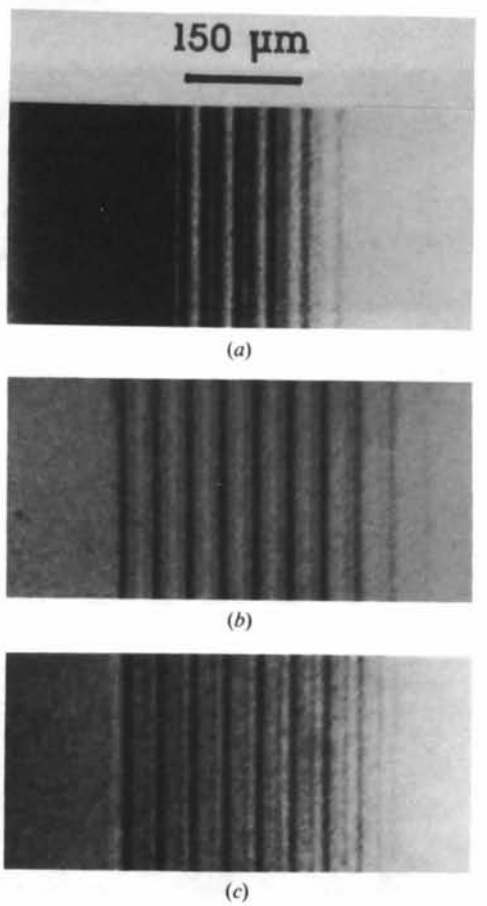

Fig. 8. Observed topographs showing the intensity distribution from the periodical relief. The pictures obtained illustrate the type-*B* diffraction setting (*cf.* Fig. 1*b*). (*a*) $\eta = -3.36$ ($\beta = 0$); (*b*) $\eta = -6.72$ ($\beta = 3.36$); (*c*) $\eta = 0$ ($\beta = -3.36$).

lar increment must be $\Delta\eta = \Lambda_0 \tan(\theta_B)/H_r$ [$\Lambda_0 = \lambda\cos(\theta_B)/\tilde{\chi}_{\mathbf{h}}$], that is $\Delta\eta \simeq 2.5$. Figs. 8(*b*) and (*c*) display topographs taken at the angular positions $\Delta\theta = \pm 3''$ ($\Delta\eta \simeq \pm 3.4$) with respect to the point at which $\beta = 0$. The nature of the interference of the patterns at these points is clearly revealed by the high contrast between intensities diffracted by the substratum and by the ridges. Shown in Fig. 9 are the simulated topographs at the pertinent angular points, obtained for the plane incident wave. To aid comprehension of how the image is formed, the relief profile, divided into specific diffraction zones, is shown schematically beneath the topographs.

Fig. 10 shows the simulated intensity profiles for the case of a ridge sufficiently high for the behavior of the interference fringes to be observed. As expected, for $|\eta| \gg 1$ (Figs. 10*a* and *b*), the period of the main maxima coincides with the limiting value [(21*a*)] and gives $D_B = 13.8\ \mu$m along the exit surface. The plane-wave solutions for the Laue–Bragg case imply that at the point $\eta = 0$ the Bloch waves in the crystal are totally reflected from the exit surface. Consequently, there must be no interference fringes at this point. Nevertheless, the computer simulation (Fig. 10*c*) shows the persistence of the interference oscillations, although their amplitude is damped with distance from the edge.

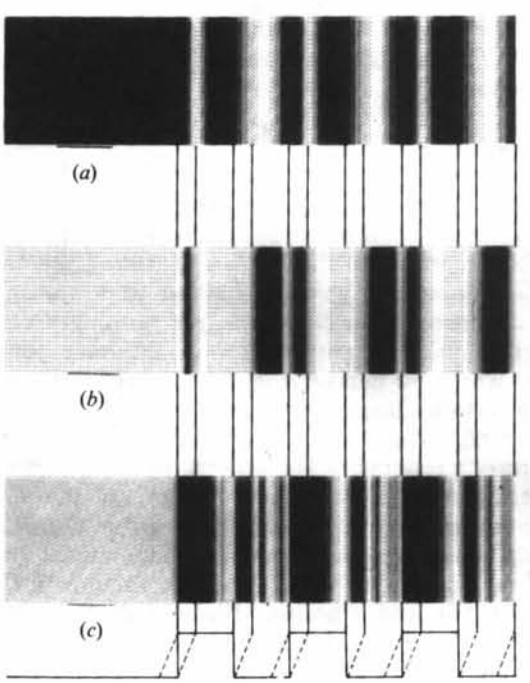

Fig. 9. Simulated topographs showing the intensity distribution from the periodical relief (three periods). The pictures illustrate the type-*B* setting (*cf.* Fig. 1*b*). (*a*) $\eta = -3.36$ ($\beta = 0$); (*b*) $\eta = -6.72$ ($\beta = 3.36$); (*c*) $\eta = 0$ ($\beta = -3.36$).

Summary

To analyze and interpret experimental results, the plane-wave solutions of the dynamic theory were used. The trouble with the plane-wave theory is that its solutions imply Bloch waves created on the infinitely extended surface and hypothetically conceivable waves on the vacuum side that are continuous with the crystal waves. For the geometries considered, the plane-wave solutions are invalid in the vicinity of the crystal edge. To obtain the true intensity distribution in the neighborhood of the edge, the computer simulation should be performed, for instance, on the basis of integral equations with the influence functions. Actually, the influence functions can be considered as the amplitudes of wave fields inside a crystal in the case of spherical-wave diffraction, when the X-ray source is located close enough to a crystal surface. Generally, the influence functions for the Laue–Bragg case coincide with those for the Bragg case. The dynamical theory of the X-ray diffraction of a spatially inhomogeneous incident wave in perfect crystals and crystals with defects, based on the use of relevant integral equations, is thoroughly described by Afanas'ev & Kohn (1971).

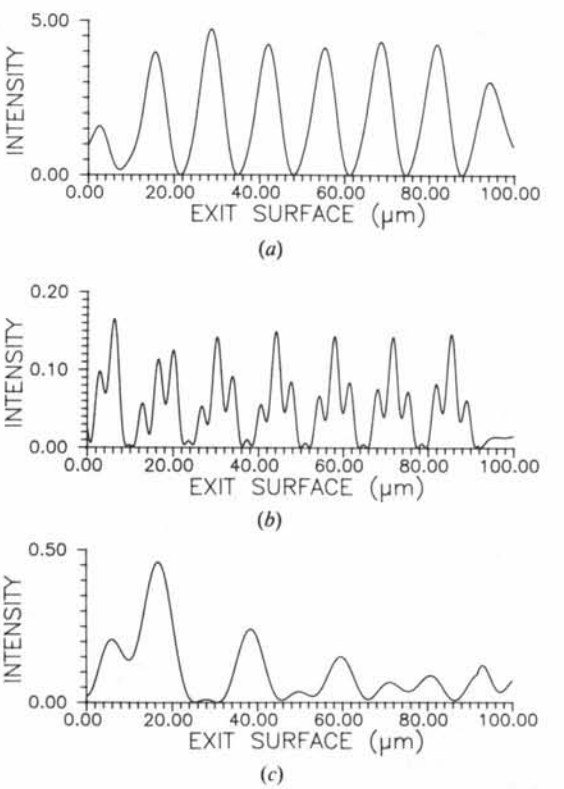

Fig. 10. Computed intensity profiles in the case of the type-*B* setting (*cf.* Fig. 1*b*). The height of the ridge $H_r = 120\ \mu$m. σ-polarization mode in all plots. (*a*) $\eta = -3.36$ ($\beta = 0$); (*b*) $\eta = -6.72$ ($\beta = 3.36$); (*c*) $\eta = 0$ ($\beta = -3.36$).

References

AFANAS'EV, A. M. & KOHN, V. G. (1971). *Acta Cryst.* A**27**, 421–430.

ARISTOV, V. V., BASOV, YU. A., GOUREEV, T. E., SNIGIREV, A. A., ISHIKAWA, T., IZUMI, K. & KIKUTA, S. (1992). *Jpn. J. Appl. Phys.* **31**, 2616–2620.

ARISTOV, V. V., WINTER, U., NIKULIN, A. YU., REDKIN, S. V., SNIGIREV, A. A., ZAUMSEIL, P. & YUNKIN, V. A. (1988). *Phys. Status Solidi A*, **108**, 651–655.

BECKER, P. & DUNSTETTER, F. (1984). *Acta Cryst.* A**40**, 241–251.

LANG, A. R., KOWALSKI, G. & MAKEPEACE, A. P. W. (1990). *Acta Cryst.* A**46**, 215–227.

LEHMANN, K. & BORRMANN, G. (1967). *Z. Kristallogr.* **125**, 234–248.

SAKA, T., KATAGAWA, T. & KATO, N. (1972*a*). *Acta Cryst.* A**28**, 102–113.

SAKA, T., KATAGAWA, T. & KATO, N. (1972*b*). *Acta Cryst.* A**28**, 113–120.

URAGAMI, T. (1969). *J. Phys. Soc. Jpn*, **27**, 147–154.

URAGAMI, T. (1970). *J. Phys. Soc. Jpn*, **28**, 1508–1527.

URAGAMI, T. (1971). *J. Phys. Soc. Jpn*, **31**, 1141–1161.

Acta Cryst. (1993). A**49**, 824–831

Peculiarities of the Low-Symmetry Phase Structure Near the Phase-Transition Point

BY G. M. CHECHIN, E. A. IPATOVA AND V. P. SAKHNENKO

Department of Physics, Rostov-on-Don University, 344090 *Rostov-on-Don, Russia*

(*Received* 5 *September* 1991; *accepted* 16 *April* 1993)

Abstract

The structure of the low-symmetry phase near the transition point depends on the number of arbitrary parameters, which is smaller than that determined by the space group G_D of this phase. Such a feature gives rise to some nontrivial structural effects in the vicinity of the transition point: there are numerical relationships among the displacements of the atoms belonging to different orbits of the G_D group. In some cases, atoms may be displaced in a direction not singled out by symmetry in any of the 230 space groups. These effects are revealed by group-theoretical methods and the Landau concept of one irreducible representation.

1. Group-theoretical methods for studying the structure of low-symmetry phases

The method of the complete condensate of order parameters (hereafter referred to as the COP method) has already been proposed for obtaining the structure of low-symmetry phases (Sakhnenko, Talanov & Chechin, 1986; Chechin, Ivanova & Saknenko, 1989). Let G be the space group of the original (high-symmetry) phase and G_D that of the low-symmetry phase that arises from the continuous structural transition $G \rightarrow G_D$ ($G_D \subset G$). The COP method allows one to obtain, for the given phase transition, the explicit form of the density function that describes the G_D phase structure in the Landau theory (Landau & Lifshitz, 1980).

The change of the density function $\delta\rho(\mathbf{r})$ for the transition $G \rightarrow G_D$ can be written as a sum of the contributions Δ_j that correspond to the different irreducible representations (IRs) Γ_j of dimension n_j of the original group G:

$$\delta\rho(\mathbf{r}) = \sum_{j=0}^{p} \Delta_j = \sum_{j=0}^{p} [\mathbf{C}_j, \mathbf{\Phi}_j(\mathbf{r})], \qquad (1.1)$$

where p is the total number of these representations. Each of the contributions Δ_j is a formal scalar product of the stationary (invariant) vector $\mathbf{C}_j = (C_j^1, C_j^2, \ldots, C_j^{nj})$, which is a multicomponent order parameter, and the vector $\mathbf{\Phi}_j = [\varphi_j^1(\mathbf{r}), \varphi_j^2(\mathbf{r}), \ldots, \varphi_j^{nj}(\mathbf{r})]$, which determines a set of the basis functions $\varphi_j^i(\mathbf{r})$ of the IR Γ_j. The stationary vector may be found from the equation

$$(\Gamma_j \downarrow G_D)\mathbf{C}_j = \mathbf{C}_j, \qquad (1.2)$$

where $\Gamma_j \downarrow G_D$ is the restriction* of the IR Γ_j of the group G to its subgroup G_D. Thus, the vector $\mathbf{C}_j$ is the common eigenvector with the eigenvalue of unity of those matrices of the IR Γ_j that correspond to all $g \in G_D$. Being the general solution to a system of homogeneous linear equations, the stationary vector depends on a certain number of arbitrary parameters, which we denote a, b, c, ... ; hence, it singles out a certain subspace in the space of the representation, whose dimension equals the number of these arbitrary parameters. The general algorithm for constructing all the stationary vectors for the Γ_j of different IRs corresponding to a given G_D phase, which constitute the complete condensate of order parameters, is given by Sakhnenko, Talanov & Chechin (1986) and Chechin, Ivanova & Sakhnenko (1989). The basis functions $\varphi_j(\mathbf{r})$ are not only determined by the IR Γ_j but also depend on the transition type (ordering, displacement *etc.*) and on

* The set of matrices of the IR Γ_j of group G corresponding to the elements of its subgroup G_D only.

©1993 International Union of Crystallography
Printed in Great Britain – all rights reserved